Journal of Materials Chemistry C

PAPER

View Article Online
View Journal | View Issue

Cite this: J. Mater. Chem. C, 2015, 3, 2054

Photoluminescence and energy transfer rates and efficiencies in Eu^{3+} activated $Tb_2Mo_3O_{12}$†

F. Baur,[a] F. Glocker[b] and T. Jüstel*[a]

Luminous efficacy (LE) and colour rendering index (CRI) of various simulated phosphor-converted warm white-light emitting diodes are calculated. Actual measured phosphor emission spectra are employed for this task. The efficacy and CRI of Eu^{3+} activated red emitting phosphors are superior to Eu^{2+} emitting nitride-based phosphors, however, Eu^{3+} suffers from low absorption strength in the blue spectral range. Tb^{3+} exhibits comparatively strong absorption in this range and can be used as a sensitizer for Eu^{3+}. A solid solution series of $(Tb_{1-x}Eu_x)_2Mo_3O_{12}$ (TM:Eu^{3+}) powders and ceramic discs is prepared by conventional solid state synthesis. Complete transfer from Tb^{3+} to Eu^{3+} is achieved in the $(Tb_{0.8}Eu_{0.2})_2Mo_3O_{12}$ sample and a red colour point is realized upon 487 nm (Tb^{3+} $^7F_6 \rightarrow {}^5D_4$) excitation with a quantum efficiency of 94%. Full conversion of a 380 nm LED and improved conversion of a 465 nm LED was achieved employing TM:Eu^{3+} ceramics. The position and temperature related shift of the Eu^{3+} Stark sublevels is determined from temperature-dependent emission and excitation spectra. These spectra also reveal excited state absorption from thermally excited Eu^{3+} $^7F_1$, $^7F_2$ and $^7F_3$ states. High-temperature measurements in the range of 350 to 800 K show a $T_{0.5}$ of 627 K. Decay measurements exhibit a clearly visible rise time. A new method to determine energy transfer rates from rise time curves is developed. From the energy transfer rates the transfer mechanism and efficiency can be determined with a higher degree of confidence compared to methods based on luminescence intensities.

Received 12th November 2014
Accepted 29th December 2014

DOI: 10.1039/c4tc02588a

www.rsc.org/MaterialsC

Introduction

Solid state lighting, especially on the basis of phosphor-converted light-emitting diodes (pcLEDs), is gaining ever increasing importance.[1–3] For the generation of white light with a high colour rendering index (CRI) generally a blue LED coated with yellow emitting YAG:Ce phosphor is used. While high luminous efficacies (LE) can be achieved with such a setup, the emitted light is cool white since almost no red light is emitted.[4] For domestic lighting application warm-white light, resembling that of incandescent light sources, is generally considered the most suitable.[5] However, introducing red emitters inevitably results in a decreased luminous efficacy due to the reduced human eye sensitivity in the red spectral range and due to a reduced package gain caused by spectral interaction between the yellow (green) and red emitting converter materials. Warm-white light sources commonly employ broad-band red emitters such as $Sr_2Si_5N_8$:Eu^{2+} and $CaAlSiN_3$:Eu^{2+}.[6] While these phosphors are highly efficient, their emission reaches into the deep red spectral range around 700 nm where the eye sensitivity is zero, resulting in a comparatively low luminous efficacy.[7,8] Therefore, the choice of the red emitting phosphor greatly influences the LE of the pcLED. It has been shown in simulations that the application of red narrow-band or line emitting phosphors is required to achieve high luminous efficacies in warm-white light emitting pcLEDs.[9–11] However, these works employed Gauss curves to simulate the phosphors' emission spectra. To the best of our knowledge there is no overview yet of the LE and CRI that can be theoretically achieved on a pcLED when applying different commercially available phosphors. Eu^{3+} activated red emitting phosphors generally exhibit high LE compared to band-emitting Eu^{2+} activated red-emitting phosphors, but they suffer from low absorption in the blue spectral range. The use of sensitizers is a suitable method to overcome such shortcomings as for example in the commercial phosphors $BaMgAl_{10}O_{17}$:Eu^{2+},Mn^{2+} or $LaPO_4$:Ce^{3+},Tb^{3+}. Eu^{3+}, however, cannot be sensitized by Ce^{3+} as a Ce^{3+}/Eu^{3+} metal-to-metal charge transfer quenches the luminescence.[3,11] The energy transfer from Tb^{3+} to Eu^{3+} is well documented in published literature, making Tb^{3+} a potential sensitizer for Eu^{3+}.[34,35,44,48–50] Tb^{3+} exhibits absorption around 487 nm, but as the underlying transition is spin- and parity forbidden as well, absorption in principal is not significantly stronger than that of Eu^{3+} itself. $Tb_2Mo_3O_{12}$ is a known host

[a]Münster University of Applied Sciences, Institute for Optical Technologies, Stegerwaldstraße 39, 48565 Steinfurt, Germany. E-mail: tj@fh-muenster.de
[b]RheinMain University of Applied Sciences, Department of Physical Engineering, Am Brückweg 26, 65428 Rüsselsheim, Germany

† Electronic supplementary information (ESI) available: CIE1931 colour points of TM:Eu^{3+} with various Eu^{3+} concentrations upon 487 nm excitation. See DOI: 10.1039/c4tc02588a

material that overcomes this limitation to some extent.[51] The Tb^{3+} concentration is high and molybdate hosts often lead to enhanced absorption strength of the 4f4f transitions.[20] This results in a comparatively strong Tb^{3+} absorption in the blue spectral range.

LED spectra calculations

In order to evaluate the value of red line emitting Eu^{3+} phosphors, we simulated spectra composed of a blue 465 nm (1000 cm^{-1}, 22 nm FWHM) LED spectrum in combination with spectra of either $Y_3Al_5O_{12}:Ce^{3+}$ (YAG:Ce) or $Lu_3Al_5O_{12}:Ce^{3+}$ (LuAG:Ce) and either $Sr_2Si_5N_8:Eu^{2+}$ (Sr258:Eu^{2+}), $CaAlSiN_3$:-Eu^{2+} (CASN:Eu^{2+}), $Tb_2Mo_3O_{12}:Eu^{3+}$ (TM:Eu^{3+}), $Li_3La_2Ba_3(MoO_4)_8:Sm^{3+}$ (LBLM:Sm^{3+}), $Mg_{14}Ge_5O_{24}:Mn^{4+}$ (MG:Mn^{4+}), or $K_2SiF_6:Mn^{4+}$ (KSF:Mn^{4+}). A second set of spectra was created by simulating the spectrum of a fully converted near-UV emitting LED (395 nm) with blue emitting $BaMgAl_{10}O_{17}:Eu^{2+}$ (BAM:Eu^{2+}) and green emitting $SrSi_2N_2O_2:Eu^{2+}$ (Sr1222:Eu^{2+}) and any one of the aforementioned red emitting phosphors. The commercially available (Sr,Ca)$AlSiN_3:Eu^{2+}$ phosphor exhibits an emission similar to $Sr_2Si_5N_8:Eu^{2+}$, so the results should be similar as well. All emission spectra were taken from self-made phosphor samples, except that of KSF:Mn^{4+} which was digitized from the Adachi and Takahashi publication.[12]

The experimental emission spectra were combined by summing their intensity values to yield simulated pcLED emission spectra. The ratio of the phosphors was adjusted to result in a spectrum with a correlated colour temperature (CCT) of 2700 K and 3000 K, respectively. The CIE1931 *x*/*y* colour points of the spectra were chosen according to ANSI C78.377 (2700 K: 0.4578/0.4101; 3000 K: 0.4338/0.4030). There is only one distinct way to combine three spectra to yield a specific colour point. For each simulated spectrum LE and CRI were calculated employing Osram Sylvania Color Calculator v4.59.[52] The results are presented in Table 1 and 2. It should be noted that the calculated LED spectra are no replacement for measurements on real pcLEDs, as potential changes of the overall spectral shape due to re-absorption processes are not considered. Moreover, we are aware of the fact that Eu^{3+} is solely weakly absorbing radiation at 465 nm since the 4f–4f transitions at this position have rather low oscillator strength. Therefore, the ratios given in the tables are not ratios for the physical amount of phosphor, but the ratio of the emission integrals on the combined spectrum. For practical application, absorption, quantum efficiencies and reabsorption would need to be taken into account. However, the results pose as a guideline as to what can theoretically be achieved when employing a certain phosphor blend.

For both Eu^{3+} and Sm^{3+} the emission only slightly depends on the host material, therefore the results should hold true for most available hosts. For the highest LE and a high CRI $Eu^{3+}$is the most suitable red emitter. Compared to CASN:Eu^{2+} an increase in LE of 31% (3000 K) or 38% (2700 K) is realized. For a high LE with an excellent CRI KSF:Mn^{4+} is the most suitable red emitter. It offers almost the same CRI as CASN:Eu^{2+} but with 25% (3000 K) or 30% (2700 K) higher LE. Sr258:Eu^{3+} and LBLM:Sm^{3+} exhibit no particularly strong advantages, but offer a good CRI with a LE higher than CASN:Eu. It should be noted that the performance of Mn^{4+} strongly depends on the host material. 660 nm emitting MGM:Mn^{4+}results in a low LE and low CRI at the same time.

To enhance the CRI of Sr258:Eu^{2+} comprising pcLEDs YAG:Ce can be substituted with LuAG:Ce. This decreases the LE but increases the CRI to close to 90. All other investigated red phosphors, with the exception of LBLM:Sm^{3+} which behaves similar to Sr258:Eu^{2+}, suffer from combination with LuAG:Ce and should be combined with YAG:Ce.

Another approach to warm-white light generation is the full-conversion near-UV LED. Its advantage is the low reabsorption since ideally all applied phosphors solely absorb in the near-UV spectral range. In this scenario Eu^{3+} offers the highest LE as well, but the CRI has decreased. Among the investigated red emitting phosphors only Sr258:Eu^{2+} and LBLM:Sm^{3+} exhibit a very good CRI of 89 and 91, respectively. The highest LE can be achieved with Eu^{3+}, at the cost of a slightly decreased CRI.

Table 1 Luminous efficacies (LE) and colour rendering indices (CRI) of various pcLEDs comprising a 465 nm blue LED at correlated colour temperatures of 2700 K and 3000 K, respectively

	2700 K			3000 K		
465 nm LED+	CRI	LE [lm W^{-1}]	Ratios (LED/Garnet/Red)	CRI	LE [lm W^{-1}]	Ratios (LED/Garnet/Red)
YAG:Ce + TM:Eu^{3+}	90	359	0.09 : 0.57 : 0.34	90	357	0.11 : 0.60 : 0.29
YAG:Ce + LBLM:Sm^{3+}	85	313	0.08 : 0.43 : 0.49	84	319	0.10 : 0.48 : 0.42
YAG:Ce + CASN:Eu^{2+}	95	260	0.06 : 0.38 : 0.56	93	272	0.08 : 0.43 : 0.49
YAG:Ce + Sr258:Eu^{2+}	85	309	0.07 : 0.43 : 0.49	84	315	0.10 : 0.48 : 0.42
YAG:Ce + MG:Mn^{4+}	78	241	0.06 : 0.40 : 0.54	83	254	0.08 : 0.44 : 0.48
YAG:Ce + KSF:Mn^{4+}	93	337	0.08 : 0.56 : 0.35	94	339	0.11 : 0.60 : 0.30
LuAG:Ce + TM:Eu^{3+}	73	345	0.06 : 0.44 : 0.50	75	343	0.09 : 0.46 : 0.46
LuAG:Ce + LBLM:Sm^{3+}	92	290	0.06 : 0.30 : 0.65	92	292	0.08 : 0.33 : 0.60
LuAG:Ce + CASN:Eu^{2+}	78	225	0.04 : 0.25 : 0.71	79	231	0.06 : 0.28 : 0.67
LuAG:Ce + Sr258:Eu^{2+}	89	283	0.06 : 0.30 : 0.64	89	286	0.07 : 0.33 : 0.60
LuAG:Ce + MG:Mn^{4+}	43	198	0.03 : 0.27 : 0.70	48	205	0.05 : 0.29 : 0.66
LuAG:Ce + KSF:Mn^{4+}	64	314	0.06 : 0.43 : 0.51	67	315	0.08 : 0.45 : 0.47

Table 2 Luminous efficacies (LE) and colour rendering indices (CRI) of various pcLEDs comprising a full-conversion UV LED at correlated colour temperatures of 2700 and 3000 K, respectively

	2700 K			3000 K		
$BAM:Eu^{2+}$ + $Sr1222:Eu^{2+}$	CRI	LE [lm W^{-1}]	Ratios (BAM/1222/Red)	CRI	LE [lm W^{-1}]	Ratio (BAM/1222/Red)
$Sr1222:Eu^{2+}$ + $TM:Eu^{3+}$	83	359	0.09 : 0.40 : 0.51	85	357	0.11 : 0.42 : 0.46
$Sr1222:Eu^{2+}$ + $LBLM:Sm^{3+}$	91	312	0.07 : 0.27 : 0.65	91	315	0.10 : 0.30 : 0.60
$Sr1222:Eu^{2+}$ + $CASN:Eu^{2+}$	84	232	0.05 : 0.23 : 0.71	85	240	0.07 : 0.26 : 0.67
$Sr1222:Eu^{2+}$ + $Sr258:Eu^{2+}$	89	305	0.07 : 0.27 : 0.65	89	308	0.10 : 0.30 : 0.60
$Sr1222:Eu^{2+}$ + $MG:Mn^{4+}$	50	205	0.05 : 0.25 : 0.70	55	214	0.06 : 0.27 : 0.67
$Sr1222:Eu^{2+}$ + $KSF:Mn^{4+}$	80	348	0.09 : 0.41 : 0.50	82	347	0.11 : 0.43 : 0.45

Experimental section

Powder samples of $(Tb_{1-x}Eu_x)_2Mo_3O_{12}$ ($TM:Eu^{3+}$) with $0 \leq x \leq 1$ were prepared by conventional solid state reactions. Stoichiometric amounts of high purity Tb_4O_7 (99.99%, Treibacher), MoO_3 (99.95%, AlfaAesar) and Eu_2O_3 (99.99%, Treibacher) were thoroughly blended in an agate mortar employing acetone as grinding medium. The resulting mixtures were dried, transferred to porcelain crucibles and calcined two times at 900 °C for 10 h in air with an intermediate grinding. After the first annealing step some particles emitting green-light or orange-light could be observed under a UV lamp in the powder, indicating the presence of pure $Tb_2Mo_3O_{12}$and $Eu_2Mo_3O_{12}$ instead of the solid solution. The second annealing step resulted in a homogeneously emitting solid solution powder. The Tb_4O_7 educt is of mixed valence, $(Tb_{0.5}^{III}Tb_{0.5}^{IV})_4O_7$, therefore requiring reduction of Tb^{4+}. Despite the low annealing temperature apparently all Tb^{4+} is reduced to Tb^{3+} as the samples exhibit a slightly yellowish body colour very unlike brownish Tb_4O_7. The reflection spectrum depicted in Fig. 3 underlines this conclusion. Ceramic discs were produced by pressing 100 mg of the synthesized powders at 0.87 GPa for two minutes in a hydraulic uniaxial press. The green bodies were sintered at 850 °C for 5 hours under air. If placed uncovered in the furnace, the ceramic discs exhibited brownish discolorations. Placing the green bodies between two alumina discs prevented the discoloration which is assumedly caused by partial oxidation of Tb^{3+} to Tb^{4+}.

XRD, fluorescence, reflection and decay measurements and temperature dependent reflection and external quantum efficiency (EQE) measurements were performed as published earlier.[13] An integration sphere with an inner shell made of Spectralon was used for room temperature reflectance and quantum efficiency measurements. The lattice parameters were calculated from XRD patterns of the synthesized powders employing STOE WinXPOW software.[14]

Results and discussion

Three modifications of $Tb_2Mo_3O_{12}$ and $Eu_2Mo_3O_{12}$ exist, the high-temperature α- and β-phases, which crystallize in the monoclinic $C12/c1$ (15) and the tetragonal $P\bar{4}21m$ (113) space group, respectively and the metastable orthorhombic $Pba2$ (32) β′ phase.[15–18,51] The melting points of the Tb and Eu compounds are 1172 and 1144 °C, respectively. The α/β-transition occurs at 835 (Tb^{3+}) and 881 °C (Eu^{3+}) while the metastable β′ phase forms at 160 (Tb^{3+}) and 180 °C (Eu^{3+}).[16] The XRD patterns depicted in Fig. 1 show that the β′ phase was obtained in this work as expected from the synthesis conditions.

The ionic radii of Tb^{3+} and Eu^{3+} differ by merely 2% and both end members crystallize in the same space group. Therefore, according to Vegard's law, a complete solid solution series should exist with a linear dependence of the lattice constants on the Tb^{3+}/Eu^{3+}concentration.[19] The unit cell volume for the synthesized powders plotted against the Eu^{3+} concentration in Fig. 2 exhibits an approximately linear behaviour. The unit cell's b and c axis are of almost the same length, rendering an exact determination from our powder samples difficult.

Both Eu^{3+} and Tb^{3+} exhibit characteristic reflection spectra in the UV and visible spectral range caused by multiple intra-configurational $[Xe]4f^6 \rightarrow [Xe]4f^6$ and $[Xe]4f^8 \rightarrow [Xe]4f^8$ transitions, respectively. All transitions are parity forbidden according to Laporte rule so their probability and absorption strength is low. However, at sufficiently high activator concentrations the lines are intense enough to be readily distinguished as depicted in Fig. 3. The reflection spectra of all samples

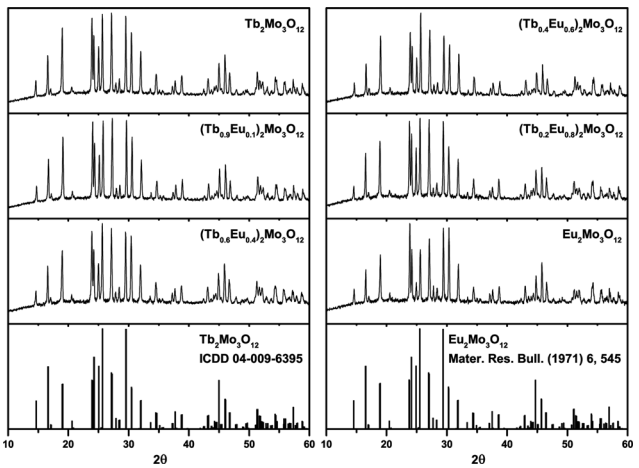

Fig. 1 XRD patterns of the synthesized $(Tb_{1-x}Eu_x)_2Mo_3O_{12}$ powders with $x = 0$, 0.1, 0.4, 0.6, 0.8, 1 and reference patterns of orthorhombic $Tb_2Mo_3O_{12}$ and $Eu_2Mo_3O_{12}$.

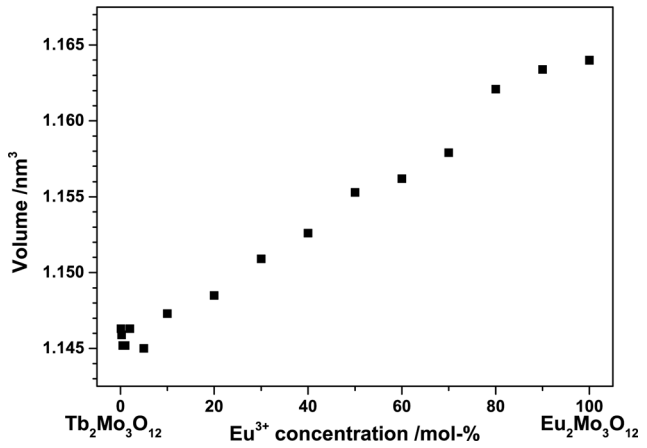

Fig. 2 Volume of the unit cell of $(Tb_{1-x}Eu_x)_2Mo_3O_{12}$ as a function of the Eu^{3+} concentration.

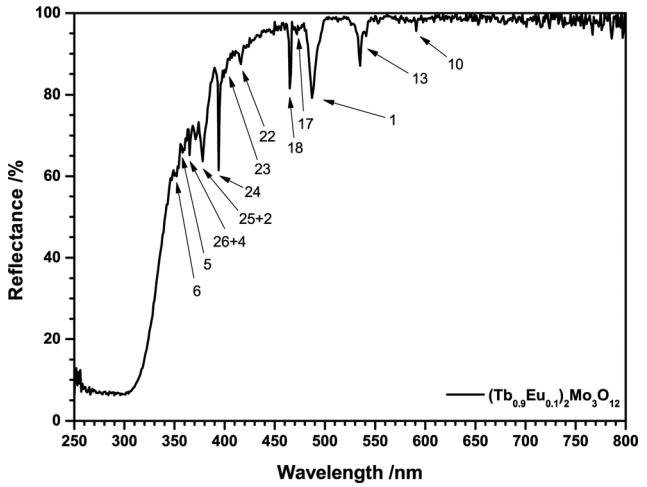

Fig. 3 Reflection spectrum of $(Tb_{0.9}Eu_{0.1})_2Mo_3O_{12}$.

consist of a broad band and several lines. Furthermore, the high reflectance in the visible range indicates high sample quality and the absence of Tb^{4+}. Incorporated Tb^{4+} would result in a brownish body colour due to a Tb^{3+}/Tb^{4+} metal-to-metal charge transfer (MMCT) as can be observed in Tb_4O_7. The broad absorption band in the UV-C to UV-B range is assigned to ligand-to-metal charge transfer (LMCT) transitions. These are essentially transitions from O^{2-} 2p to Mo^{6+} 4d or to Eu^{3+} 5d bands or orbitals and are commonly observed in Eu^{3+} doped molybdates.[20–22] DOS calculations have shown that a 4d band of Mo^{6+} in molybdates is often located around 4 eV, matching the spectral region of the observed absorption band.[23,24] Such transitions are spin and parity allowed and result in high absorption. Efficient excitation is possible *via* O^{2-}/Eu^{3+} LMCT transitions and this mechanism has been widely applied in fluorescent lamps to excite Eu^{3+} in oxides.[25,26] Contrary to that, the O^{2-}/Mo^{6+} LMCT is often partly quenched at room temperature, resulting in poor excitability in that spectral region.[53]

In today's commercial pcLEDs the excitation wavelength is either around 400 nm for near-UV LEDs or around 450 nm for blue LEDs,[4,27] *i.e.* excitation *via* the CT bands is not possible. The Eu^{3+} activated samples exhibit two prominent absorption lines at 394 nm and 465 nm, originating from the $^7F_0 \rightarrow {}^5L_6$ and $^7F_0 \rightarrow {}^5D_2$ transitions. While the energy of these transitions fits to the emission spectra of near-UV and blue LED chips very well, the low absorption cross-section hinders an efficient application in phosphor converted LEDs (pcLEDs). Trivalent Terbium exhibits a relatively broad and strong line absorption multiplet peaking at 487 nm with a FWHM of 10 nm. This broad absorption can be assigned to transitions from the $^7F_6$ ground state to the $^5D_4$ state. The ligand field generated by the O^{2-} ligands lifts the m_j degeneracy of both states.[28] Due to the symmetry of the dopant sites each $\pm m_j$ pair is degenerate, so that for an odd number of f-electrons $J + 1$ distinct levels emerge, *i.e.* 7 and 5, respectively. The large number of potential transitions from and to the ground and excited state sublevels explains the observed broad absorption line.

The excitation spectra as depicted in Fig. 4 exhibit the different transitions of single and co-doped samples. As discussed earlier the broad structured band between 250 and 350 nm is attributed to the $O^{2-} \rightarrow Mo^{6+}$ and Eu^{3+} LMCT, respectively. Due to the higher positive charge and reduction potential of Mo^{6+}, the low-energy shoulder is assigned to Mo^{6+} LMCT, while the high-energy shoulder is assigned to Eu^{3+} LMCT. However, the $Tb_2Mo_3O_{12}$ sample (a) exhibits a band apparently consisting of two components as well. Since no Eu^{3+} is present and the emission at 541.5 nm was monitored, this cannot be ascribed to a Eu^{3+} LMCT. The Tb^{3+} LMCT is at much higher energies, however, the lowest 4f–5d transition of Tb^{3+} is reported to be located around 275 nm in $[TbCl_6]^{3-}$.[29] Therefore, this high-energy shoulder is tentatively assigned to a Tb^{3+} 4f–5d transition. The excitation of the $Tb_2Mo_3O_{12}$ sample (a) was measured monitoring the green 541.5 nm emission of Tb^{3+}. Peaks that could be attributed to specific transitions were assigned a number that can be found in Table 3 and Fig. 5. The Tb^{3+} excitation spectrum shows the $^7F_6 \rightarrow {}^5D_4$ transition as a prominent feature as depicted in Fig. 4. Similarly the observed transitions in the $Eu_2Mo_3O_{12}$ sample (c), monitored at the red 615 nm emission of Eu^{3+} were assigned numbers which are

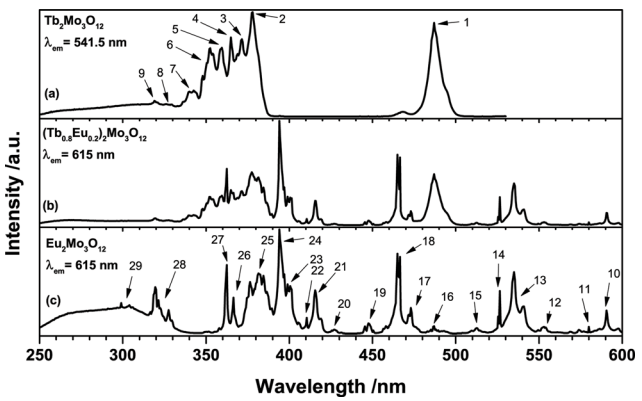

Fig. 4 Excitation spectra of (a) $Tb_2Mo_3O_{12}$, (b) $(Tb_{0.6}Eu_{0.4})_2Mo_3O_{12}$ and (c) $Eu_2Mo_3O_{12}$ with emission monitored at 541.5 nm and 615 nm, respectively.

Table 3 Tb^{3+} (1–9) and Eu^{3+} (10–29) intraconfigurational transitions with their respective peak wavelengths, wavenumber and number assigned for reference in illustrations in this work

Number	Wavelength/ nm	Wavenumber/ 10^3 cm^{-1}	Transitions
1	487	20.5	$^7F_6 \rightarrow {}^5D_4$
2	378	26.5	$^7F_6 \rightarrow {}^5D_3$
3	371.5	26.9	$^7F_6 \rightarrow {}^5L_{10}$
4	363–369	27.1–27.5	$^7F_6 \rightarrow {}^5G_6 + {}^5L_9 + {}^5G_5$
5	359.5	27.8	$^7F_6 \rightarrow {}^5D_2$
6	348–355	28.2–28.7	$^7F_6 \rightarrow {}^5L_8 + {}^5G_4 + {}^5L_7$
7	336–345	29.0–29.8	$^7F_6 \rightarrow {}^5L_6 + {}^5G_3 + {}^5G_2$
8	~326	~30.7	$^7F_6 \rightarrow {}^5D_1$
9	319	31.3	$^7F_6 \rightarrow {}^5D_0$
10	590.5	16.9	$^7F_1 \rightarrow {}^5D_0$
11	580	17.2	$^7F_0 \rightarrow {}^5D_0$
12	553	18.1	$^7F_2 \rightarrow {}^5D_1$
13	535	18.7	$^7F_1 \rightarrow {}^5D_1$
14	526.5	19.0	$^7F_0 \rightarrow {}^5D_1$
15	512.5	19.5	$^7F_3 \rightarrow {}^5D_2$
16	487	20.5	$^7F_2 \rightarrow {}^5D_2$
17	473	21.1	$^7F_1 \rightarrow {}^5D_2$
18	465	21.5	$^7F_0 \rightarrow {}^5D_2$
19	447.5	22.3	$^7F_3 \rightarrow {}^5D_3$
20	427	23.4	$^7F_2 \rightarrow {}^5D_3$
21	415	24.1	$^7F_1 \rightarrow {}^5D_3$
22	411	24.3	$^7F_0 \rightarrow {}^5D_3$
23	398–402	24.9–25.1	$^7F_0 \rightarrow {}^5L_6$
24	394	25.4	$^7F_0 \rightarrow {}^5L_7$
25	371–390	25.6–27.0	$^7F_0 \rightarrow {}^5L_8 + {}^5G_j + {}^5L_9 + {}^5L_{10}$
26	366.5	27.3	$^7F_1 \rightarrow {}^5D_4$
27	362.5	27.6	$^7F_0 \rightarrow {}^5D_4$
28	315–332	30.1–31.7	$^7F_0 \rightarrow {}^5H_j$
29	297–306	32.7–33.7	$^7F_0 \rightarrow {}^5F_j + {}^5I_j$

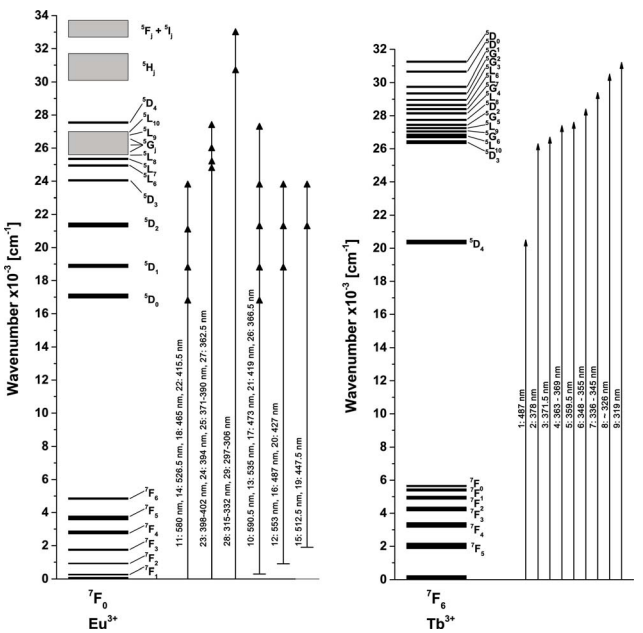

Fig. 5 Fraction of the energy level diagram of Eu^{3+} and Tb^{3+} with observed transitions, created from Dieke.[32]

included in Table 3 and Fig. 5. While all transitions of Tb^{3+} seem to originate from the $^7F_6$ ground state, in the $Eu_2Mo_3O_{12}$ excitation spectra transitions that apparently originate from the excited $^7F_1$, $^7F_2$, and $^7F_3$ states can be observed. According to Boltzmann equation, weighted with the respective number of degenerate states,[30] the percentile population at 297 K of the four lowest-lying ^7F_J levels in TM:Eu^{3+} is 68.9%, 28.6%, 2.49% and 0.015%, respectively. The $^7F_3$ level is merely slightly populated and among the potential transitions only the $^7F_3 \rightarrow {}^5D_3$ can be observed as a weak line multiplet centred at 447.5 nm. This can be explained by the transition being partially allowed due to $\Delta J = 0$.

To further investigate this finding, temperature dependent excitation spectra of the red 615 nm emission of $Eu_2Mo_3O_{12}$ were recorded (Fig. 6). Lines that were assigned to transitions from excited states increase in intensity with increasing temperature while those originating from $^7F_0$ transitions decrease with increasing temperature due to thermal quenching of the emission. Furthermore, the $^7F_0$ lines exhibit a blue-shift with increasing temperature as depicted in the inset of Fig. 6. The inset shows the lines attributed to the $^7F_J \rightarrow {}^5D_0$ ($J = 0$, 1) transitions, respectively. The $^7F_0 \rightarrow {}^5D_0$ transition around 580 nm is strongly forbidden due to $J = 0 \Leftrightarrow 0$ and is therefore of weak intensity. The observed blue shift is the same for all $^7F_0$ transitions and can be quantified to approximately 20 cm^{-1} from 100 to 500 K or 0.05 cm^{-1} K^{-1}. The $^7F_1 \rightarrow {}^5D_0$ transition around 591 nm exhibits no such shift as do none of the other transitions originating from either $^7F_1$ or $^7F_2$. Therefore, we conclude that the $^7F_0$ ground state shifts to lower energy while the excited states remain at their respective energy position. Furthermore, a red-shift of the $O^{2-} \rightarrow Mo^{6+}$ LMCT band can be observed with increasing temperature. A phase-transition can be ruled out as the cause as the shift progresses steadily within the 100 to 500 K range and the $\beta \rightarrow \beta'$ transition occurs around 450 K.[16] The orthorhombic $Ln_2Mo_3O_{12}$ phase seems to possess negative thermal expansion coefficient according to Xiao *et al.*[31] Though charge transfer transitions are not as sensitive to distance changes, the decreased O^{2-}/Mo^{6+} distance could explain the observed red-shift.

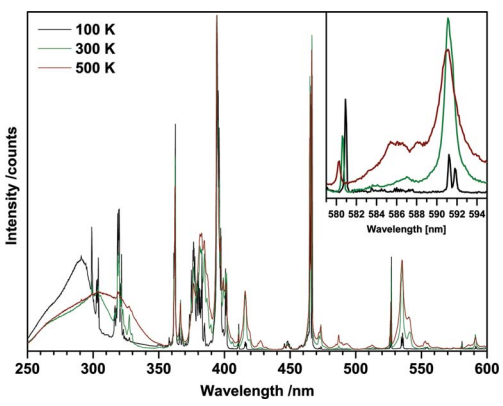

Fig. 6 Temperature dependent excitation spectra of $Eu_2Mo_3O_{12}$ monitoring the red 615 nm emission of Eu^{3+}. The inset depicts the $^7F_0 \rightarrow {}^5D_0$ and $^7F_1 \rightarrow {}^5D_0$ transition lines.

At 100 K the lines can be resolved to their respective Stark components. The inset of Fig. 6 depicts this for the $^7F_1 \rightarrow {}^5D_0$ transition. The $^7F_1$ level is split into $J + 1 = 2$ distinct Stark sublevels, resulting in two transitions peaking at 591.2 nm and 591.8 nm, respectively. Similarly, the $^7F_1 \rightarrow {}^5D_1$ transition around 535 nm results in four lines, since both states are split into two distinct sublevels. From the spectral positions of the peaks of the four $^7F_0 \rightarrow {}^5D_J$ ($J = 0, 1, 2, 3$) transitions the energy positions of the Stark sublevels of $^5D_0$, $^5D_1$, $^5D_2$ and $^5D_3$ were determined. The energetic position of the two $^7F_1$ sublevels were calculated by applying these values to the spectral positions of the peaks of the two $^7F_1 \rightarrow {}^5D_{0,1}$ transitions in the excitation spectrum. The determination of $^7F_2$ sublevels was not possible since due to the large number of transitions involved the individual peaks could not be sufficiently discerned. The obtained values are listed in Table 4. The accuracy of the absolute values is at least 0.5 nm, corresponding to 30 to 15 cm^{-1}, depending on the spectral position. The relative accuracy, *i.e.* the positions of the sublevels relative to each other is 0.1 nm, corresponding to 6 cm^{-1} or less.

Table 4 Energy of the Stark sublevels of the ^7F_J ($J = 0, 1$) and ^5D_J ($J = 0, 1, 2, 3$) of Eu^{3+}

Level	m_j	Energy [cm^{-1}]
$^7F_0$		0
$^7F_1$	0	307
	±1	323
$^5D_0$	0	17 215
$^5D_1$	0	18 968
	±1	19 001
$^5D_2$	0	21 492
	±1	21 468
	±2	21 422
$^5D_3$	0	24 337
	±1	24 355
	±2	24 372
	±3	24 393

Emission spectra of $(Tb_{1-x}Eu_x)_2Mo_3O_{12}$ ($0 < x < 1$) upon 487 nm excitation were recorded and are presented in Fig. 7(a). The 487 nm radiation excites the $^7F_6 \rightarrow {}^5D_4$ transition in Tb^{3+}. The corresponding $^5D_4 \rightarrow {}^7F_5$ emission peaking at 541.5 nm can be observed in all spectra, but decreases in intensity with increasing Eu^{3+} concentration. At $x > 0.2$ the green Tb^{3+} emission is completely quenched. Even at low concentrations such as $x = 0.001$ Eu^{3+} emission can be observed, indicating a highly efficient Tb^{3+} to Eu^{3+} energy transfer. The dominant peaks of the Eu^{3+} emission are located around 590 nm, 615 nm, and 700 nm, corresponding to transitions from $^5D_0$ to ^7F_J ($J = 1, 2, 4$), respectively. The nature of the Eu^{3+} emission will be discussed in more detail later in this work. Upon exciting at 487 nm *via* Tb^{3+}, the Eu^{3+} emission intensity increases with increasing Eu^{3+} concentration until a maximum is reached at 20% after which the intensity starts to decreases. This is mainly caused by the decreasing Tb^{3+} concentration and consequent decreasing absorption in the 487 nm range. A second potential factor is concentration quenching of the Eu^{3+} emission. To disentangle these two phenomena the emission was recorded upon 465 nm excitation which directly excites the Eu^{3+} ions ($^7F_0 \rightarrow {}^5D_3$) and eliminates the influence of the energy transfer on the emission intensity. The spectra are presented in Fig. 7(b). If Eu^{3+} is directly excited the highest emission intensity can be achieved for the sample comprising 60% Eu^{3+}.

To determine the thermal quenching (TQ) behaviour of TM:Eu^{3+}, emission spectra of $(Tb_{0.6}Eu_{0.4})_2Mo_3O_{12}$ were recorded in the range of 350 to 800 K with a high temperature sample holder. Similar to the temperature-dependent excitation spectra, a blue-shift of some of the Stark sublevels with increasing temperature could be observed (Fig. 8(a)). This is attributed to lattice contraction and an increase of the strength of the ligand field influencing the central Eu^{3+} ion. This causes

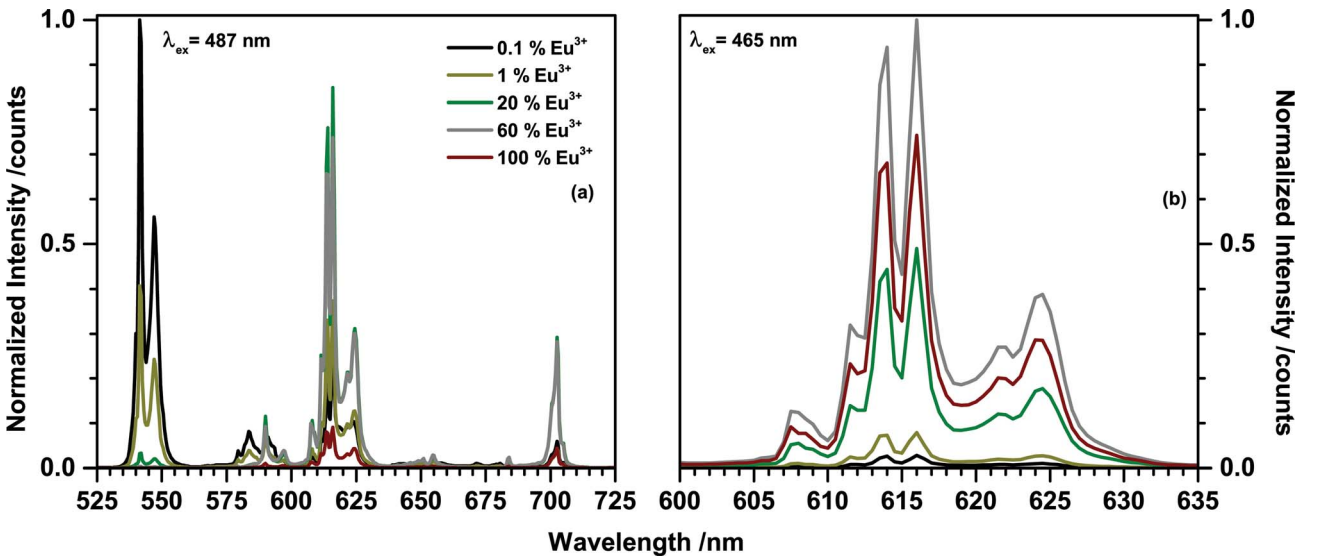

Fig. 7 Emission spectra of $(Tb_{1-x}Eu_x)_2Mo_3O_{12}$ with different Eu^{3+} concentrations upon (a) 487 nm excitation and (b) 465 nm excitation.

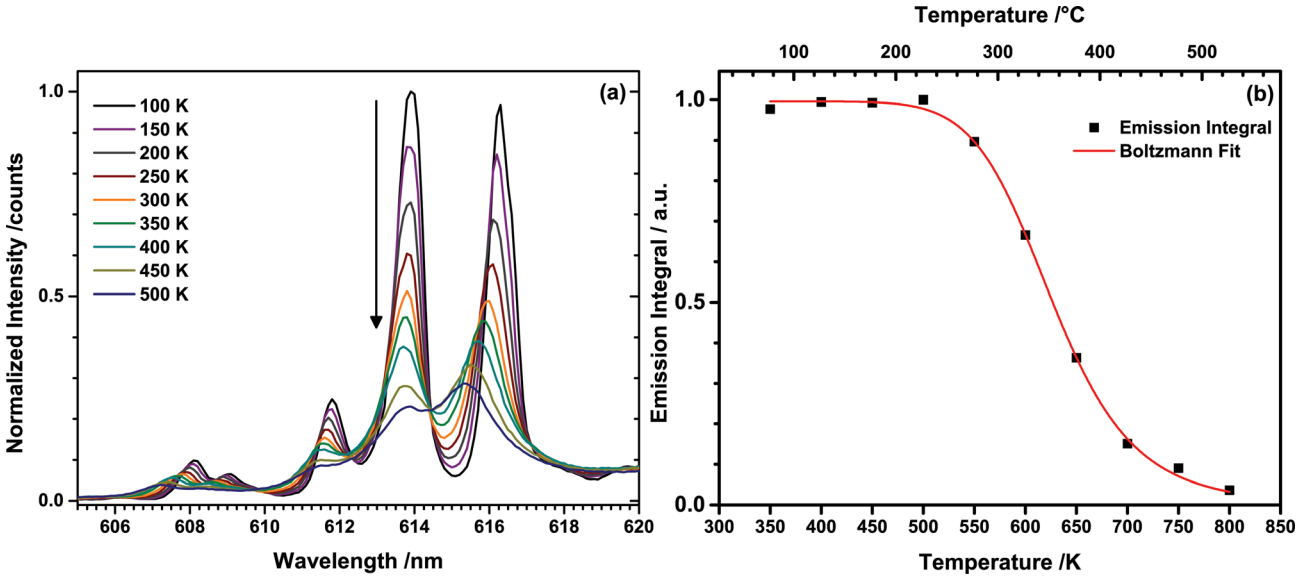

Fig. 8 (a) Temperature dependent emission spectra of the $^5D_0 \rightarrow {}^7F_2$ transition of Eu^{3+} upon 487 nm excitation (Tb^{3+}) and (b) integrated emission intensities with the corresponding Boltzmann fit.

an increase of the Stark splitting and consequently of the energy distance between the $^5D_0$ and some of the ^7F_J sublevels.

Emission intensities in the range of 550–800 nm were integrated and plotted over the temperature as depicted in Fig. 8(b). The emission intensity remains constant up to a temperature of 500 K, while at higher temperature thermal quenching sets in. The normalized data points were fitted with the Boltzmann equation

$$I(T) = \frac{I_0}{1 + B\mathrm{e}^{\frac{-E_A}{kT}}} \quad (1)$$

where I_0 is the initial intensity, being equal to 1 here, B is the quenching frequency factor and E_A is the energy required to activate the thermal quenching process. The fit as depicted in Fig. 8(b) resulted in $E_A = 0.84$ eV $\pm$ 0.04 eV which corresponds to a $T_{0.5}$ of approximately 627 K. The relative emission intensity at 400 K, I_{400}, corresponding to the performance at the average work temperature of a high-power LED, equals 99.6%. The temperature at which the relative emission intensity has decreased to 90%, T_{90}, equals to 548 K. This excellent temperature stability renders TM:Eu^{3+} a promising candidate for warm-white pcLEDs.

To investigate the LED performance of TM:Eu^{3+}, a $(Tb_{0.6}Eu_{0.4})_2Mo_3O_{12}$ ceramic disc (0.4 mm thickness) was placed on a 380 nm UV-emitting LED and a 465 nm blue LED, respectively. Fig. 9(a) depicts the emission spectrum of the 380 nm LED and Fig. 9(b) shows the spectrum of the same LED behind a $(Tb_{0.6}Eu_{0.4})_2Mo_3O_{12}$ ceramic disc. The 380 nm LED excites both Tb^{3+} and Eu^{3+}. Tb^{3+} absorbs mainly *via* the $^7F_6 \rightarrow {}^5D_3$ and $^5L_{10}$ transitions at 378 nm and 372 nm, respectively. Eu^{3+} absorbs *via* the $^7F_0 \rightarrow {}^6L_8$ and $^6L_7$ transitions at 394 nm and 399 nm, respectively. Almost full conversion of the UV radiation could be achieved, resulting in an orange-red CIE1931 colour point of $x = 0.641, y = 0.325$. Fig. 9(c) and (d) depict the emission spectra of a blue 465 nm LED and of the same LED behind the $(Tb_{0.6}Eu_{0.4})_2Mo_3O_{12}$ ceramic disc. The blue LED emission is absorbed by both Tb^{3+} and Eu^{3+}. The involved transitions are Tb^{3+} $^7F_6 \rightarrow {}^5D_4$ (487 nm) and Eu^{3+} $^7F_0 \rightarrow {}^5D_2$ (465 nm) and to a lesser extend Eu^{3+} $^7F_1 \rightarrow {}^5D_2$ (473 nm). The CIE 1931 colour point is in the purple region with $x = 0.213$, $y = 0.114$.

In both LEDs TM:Eu^{3+} exhibits increased absorption strength compared to a non-sensitized Eu^{3+} phosphor due to the simultaneous absorption by $Tb^{3+}$and Eu^{3+}. No Tb^{3+} emission could be observed due to the very efficient energy transfer to Eu^{3+}.

External quantum efficiencies (EQE) were determined for excitation at 465 nm (Eu^{3+} excitation) and 487 nm (Tb^{3+} excitation). Here, the EQE is defined as

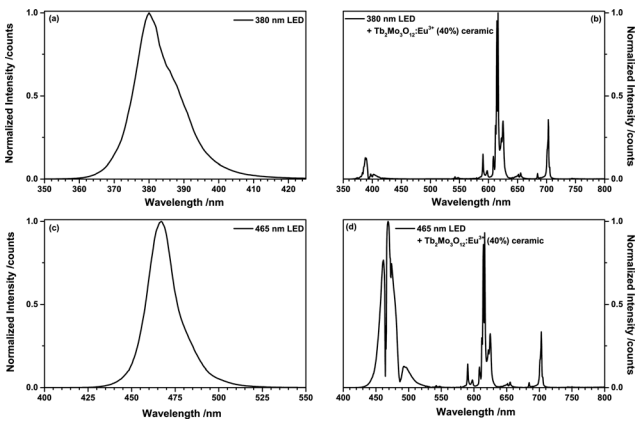

Fig. 9 (a) Emission spectrum of a 380 nm LED and (b) emission spectrum of the same 380 nm LED behind a $(Tb_{0.6}Eu_{0.4})_2Mo_3O_{12}$ ceramic disc. (c) Emission spectrum of a 465 nm LED and (d) emission spectrum of the same 465 nm LED behind a $(Tb_{0.6}Eu_{0.4})_2Mo_3O_{12}$ ceramic disc.

$$\mathrm{EQE} = \frac{N_{\text{absorbed photons}}}{N_{\text{emitted photons}}} \quad (2)$$

The results are listed in Table 5. The EQE increases with increasing Eu^{3+} concentration until it reaches a maximum of 94% at 20% Eu^{3+}. At low Eu^{3+} concentrations the fraction of photons absorbed by the host structure without conversion to red light is comparatively large, resulting in the observed lower EQE. Increasing the Eu^{3+} concentration further results in a decrease of EQE. This is attributed to concentration quenching. The emission spectrum of the 20% Eu^{3+} sample already possesses a red colour point with hardly any green Tb^{3+} emission visible. Therefore, TM:Eu^{3+} (20%) is the most promising sample of the concentration series, combining a high EQE with a red colour point.

Decay curve measurements for the Eu^{3+} $^5D_2 \rightarrow {}^7F_2$ emission around 615 nm upon 487 nm (Tb^{3+} $^7F_6 \rightarrow {}^5D_4$) excitation presented in Fig. 10(a) revealed the existence of a pronounced rise time of the Eu^{3+} emission. The established term rise time describes the phenomenon that the emission intensity increases for a period of time following excitation. In the diagram it is visible as a rising of the decay curves in the range of 10^{-4} s. The emission intensity measured in a decay experiment is proportional to the number of excited activator ions. Therefore, an increase of the emission intensity implicates an increase in the number of excited activator ions over time. Since the excitation source is switched off at the beginning of a decay measurement, this phenomenon indicates some sort of energy transfer. Either within the activator ion, *i.e.* from one excited state to the other or between two separate ions. Upon 465 nm excitation (Eu^{3+} $^7F_0 \rightarrow {}^5D_2$) no rise time could be observed (Fig. 10(b)). Therefore, the rise time is caused by energy transfer from Tb^{3+} to Eu^{3+}. As depicted in Fig. 10(a) the length of the rise time decreases with increasing Eu^{3+} concentration due to decreasing mean minimal sensitizer and activator distance. The decay time of Eu^{3+} decreases independent of the excitation pathway, which is caused by concentration quenching and reflects the decreasing internal quantum efficiency (IQE). The IQE is defined here as the probability of the occurrence of a radiative transition to the ground state as opposed to that of a non-radiative relaxation and is proportional to the decay time. The value differs from the EQE in so far as losses occurring due to competing absorption processes and reabsorption of generated photons in the material are disregarded. The sample possessing the highest IQE is the 0.1% Eu^{3+} sample contrary to the 20% sample possessing the highest EQE. This demonstrates the influence of host absorption on the EQE of activators with low absorption coefficients. Several attempts to determine the energy transfer rate from rise time curves can be found in literature.[33–38]

However, these models are only valid if a complete energy transfer occurs from the sensitizer to the activator, *i.e.* a transfer efficiency of $\eta_{ET} = 1$. This is obviously not the case for TM:Eu^{3+} with Eu^{3+} concentrations lower than 20% as Tb^{3+} emission can be observed. Therefore, the following differential equations are used to model the decay behaviour:

Table 5 Quantum efficiency of TM:Eu^{3+} with different activator concentration upon 465 nm and 487 nm excitation

Eu^{3+} concentration [%]	EQE (λ_{ex} = 465 nm)	EQE (λ_{ex} = 487 nm)
0		74
1	56	80
5	70	89
10	74	85
20	73	94
40	75	80
50	63	72
60	65	67
80	46	48
100	48	

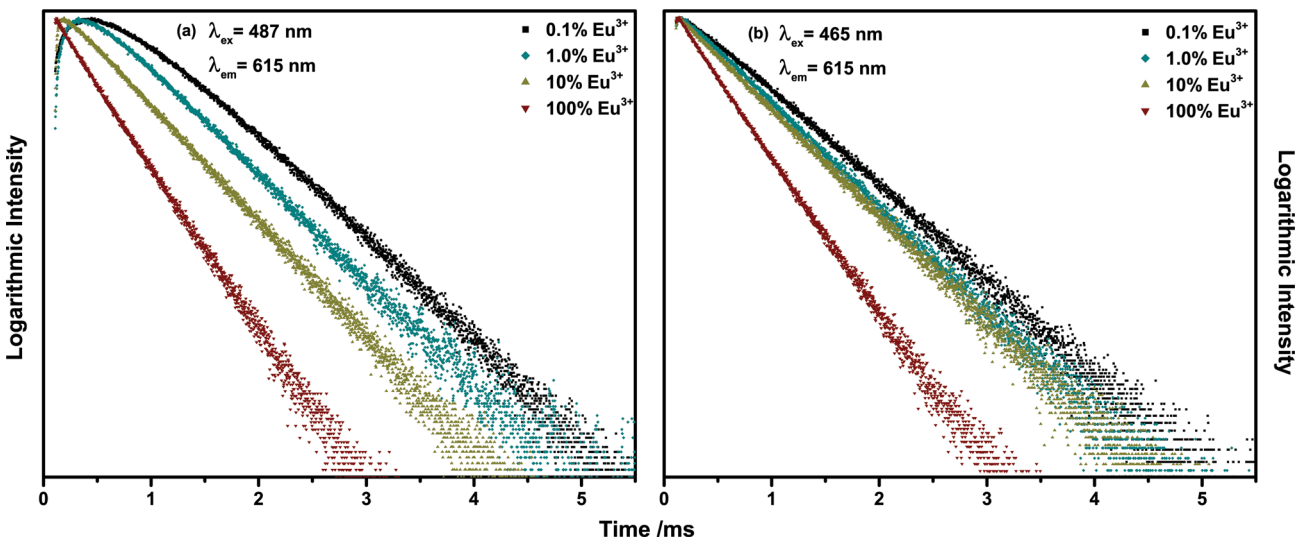

Fig. 10 Decay curves of 615 nm emission of $(Tb_{1-x}Eu_x)_2Mo_3O_{12}$ with x = 0.001, 0.01, 0.1, 1 under (a) 487 nm and (b) 465 nm excitation.

$$\frac{dN_{Tb}}{dt} = -(ET_{Tb,Eu} + \lambda_{Tb})N_{Tb} \quad (3)$$

$$\frac{dN_{Eu}}{dt} = +ET_{Tb,Eu}N_{Tb} - \lambda_{Eu}N_{Eu} \quad (4)$$

N_{Tb} and N_{Eu} are the number of excited Tb^{3+} and Eu^{3+} ions, respectively. $ET_{Tb,Eu}$ is the rate of the energy transfer from Tb^{3+} to Eu^{3+}. $\lambda_{Tb}$and λ_{Eu} are the combined rates of non-radiative and radiative transitions to the ground state of the respective ion. Solving the differential equations results in

$$N_{Eu}(t) = C_2 e^{-\lambda_{Eu}t} - \frac{C_1 ET_{Tb,Eu}}{(ET_{Tb,Eu} + \lambda_{Tb}) - \lambda_{Eu}}\left[e^{-(ET_{Tb,Eu}+\lambda_{Tb})t} - e^{-\lambda_{Eu}t}\right] \quad (5)$$

There is no unique solution to this function when fitting a decay curve. It is only possible to determine the sum of $ET_{Tb,Eu}$ and λ_{Tb} but not their separate values. However, eqn (5) can be simplified to

$$N_{Eu}(t) = -C[e^{-\lambda_{Tb,total}t} - e^{-\lambda_{Eu}t}] \quad (6)$$

where $\lambda_{Tb,total} = ET_{Tb} + \lambda_{Tb}$. It was also assumed that $C_2 \approx 0$ as the number of directly excited Eu^{3+} ions will be very small compared to those excited by energy transfer when irradiating with 487 nm. A single parameter C can be used instead of the fraction in eqn (5) as parameter C_1 can take any value and therefore the value of the fraction is independent of any of the other parameters. Employing eqn (6) to fit the decay curves yields three parameters: C, $\lambda_{Tb,total}$ and λ_{Eu}. Parameter C has no purposeful meaning as it is strongly influenced by the measurement setup. λ_{Eu} is the decay rate of Eu^{3+} and $\lambda_{Tb,total}$ is the decay rate of Tb^{3+}, being the sum of $ET_{Tb,Eu}$ and λ_{Tb}, the rate of energy transfer and the rate of radiative decay of Tb^{3+}.

To extract the energy transfer rate $ET_{Tb,Eu}$ from $\lambda_{Tb,total}$ two methods can be employed. One way is to derive it from the energy transfer efficiency η_{ET}, which is defined as the ratio of the energy transfer rate to the total decay rate:

$$\eta_{ET} = \frac{ET_{Tb,Eu}}{\lambda_{Tb,total}} \quad (7)$$

$$ET_{Tb,Eu} = \lambda_{Tb,total}\eta_{ET} \quad (8)$$

The energy transfer efficiency η_{ET} is frequently calculated from either luminescence intensities or lifetimes by employing equations

$$\eta_{ET} = 1 - \frac{\tau_s}{\tau_{s0}} \quad (9)$$

$$\eta_{ET} = 1 - \frac{I_s}{I_{s0}} \quad (10)$$

where τ_s and I_s are the luminescence life times and intensities, respectively, of the sensitizer in presence of the activator and τ_{s0} and I_{s0} are those in absence of the activator.[39,40] In case of TM:Eu^{3+}, however, these methods cannot be employed as they assume a constant sensitizer concentration, whereas here the sensitizer concentration decreases with increasing activator concentration.

Therefore, the ratio of $ET_{Tb,Eu}$ and λ_{Tb} was approximated from emission spectra. Under the assumption that all Eu^{3+} emission stems from energy transfer from Tb^{3+}, the emission integral of Eu^{3+} is proportional to $ET_{Tb,Eu}$. Furthermore, the emission integral of Tb^{3+} can be assumed to be proportional to λ_{Tb}. Consequently, the ratio of the emission integrals of Tb^{3+} and Eu^{3+} will be equal to the ratio of λ_{Tb} and $ET_{Tb,Eu}$, henceforth denoted as R_{ET}.

$$I_{Eu} \propto ET_{Tb,Eu} \wedge I_{Tb} \propto \lambda_{Tb} \Rightarrow \frac{I_{Tb}}{I_{Eu}} = \frac{\lambda_{Tb}}{ET_{Tb,Eu}} =: R_{ET} \quad (11)$$

Considering that

$$\lambda_{Tb} + ET_{Tb,Eu} = \lambda_{Tb,total},$$

from eqn (7) and (11) follows

$$ET_{Tb,Eu} = \frac{\lambda_{Tb,total}}{1 + R_{ET}} \quad (12)$$

Energy transfer rates were calculated with eqn (12). In Fig. 11 the energy transfer rate and the energy transfer efficiency are plotted in dependence on the Eu^{3+} concentration. The transfer rate increases steadily due to a decreasing mean minimal distance from Tb^{3+} to Eu^{3+} while the efficiency converges to unity. No rate could be calculated for the 80% sample as the rise time can hardly be observed in that case due to its very short duration.

Energy transfer can occur either by exchange interaction or multipolar interaction.[41] Exchange interaction is generally assumed to occur only if the mutual separation between sensitizer and activators ions is not larger than about 0.3 nm.[42,43] Generally, Blasse's equation is employed to determine the critical distance of the energy transfer.[44–47] However, the equation uses the sum of sensitizer and activator concentration

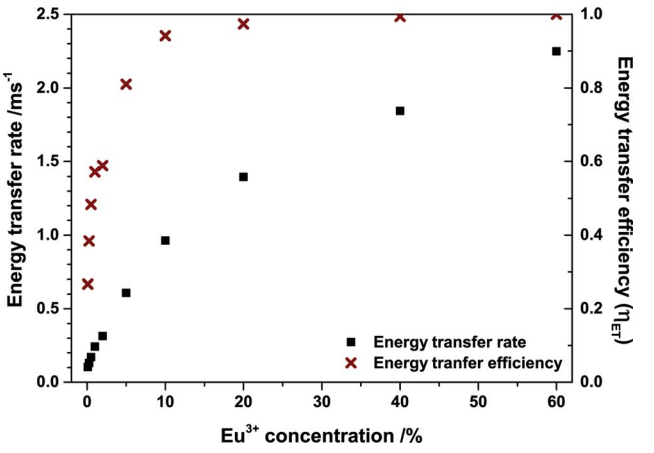

Fig. 11 Energy transfer rate and efficiency of $(Tb_{1-x}Eu_x)_2Mo_3O_{12}$ at different Eu^{3+} concentrations.

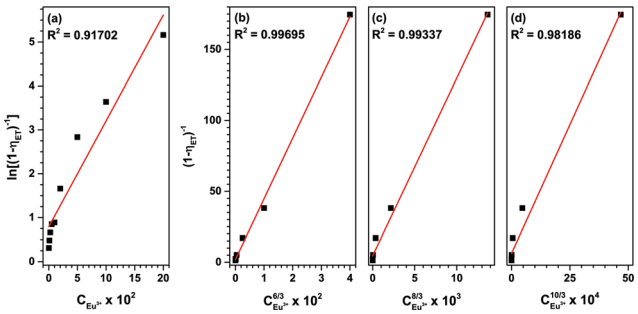

Fig. 12 Dependence of energy transfer rates on (a) $C_{Eu^{3+}}{}^{6/3}$, (b) $C_{Eu^{3+}}{}^{8/3}$ and (c) $C_{Eu^{3+}}{}^{10/3}$ and (d) the dependence of $\ln(I_0/I\ (Tb^{3+}))$ on $C_{Eu}{}^{3+}$.

and effectively calculates the mean minimum distance within the combined group of sensitizer and activator ion and not the mean minimum distance from the sensitizer to the activator. In case of TM:Eu^{3+} the calculated distance does not change as Eu^{3+} substitutes Tb^{3+} and the sum remains unity. Another method to approximate the energy transfer mechanism is by employing the distance dependence of the energy transfer efficiency.

To disentangle the relation of transfer efficiency and sensitizer–activator distance in a given material, I_0/I or τ_0/τ are frequently plotted against the concentration of the activator ion.[44–47] This stems from the relations $\frac{\eta_0}{\eta} \propto C^{n/3}$ for multipolar interaction and $\left(\frac{\eta_0}{\eta}\right)^e \propto C$ for exchange interaction. These relations were approximated by Reisfeld from Dexter's calculations.[41] From eqn (10) follows that I_0/I value is equal to $\frac{1}{1-\eta_{ET}}$. By employing the values for η_{ET} obtained from fitting the rise time curves, the plots depicted in Fig. 12 were attained.

These plots depict the proportionality of the energy transfer efficiency to the Eu^{3+} concentration to the power of 1, 6/3, 8/3 and 10/3, respectively. An R^2 of 0.997 was achieved for $C^{6/3}$, strongly pointing at a dipole–dipole ET mechanism. This is in good agreement with the published literature on Tb^{3+} to Eu^{3+} energy transfer.[33,44,48]

Conclusions

In warm-white pcLEDs the highest LE and very good CRI values can be achieved by employing Eu^{3+} activated phosphors as the red emitter. While Eu^{3+} suffers from weak absorption in the blue and near-UV spectral region, $Tb_2Mo_3O_{12}$:Eu^{3+} shows increased absorption in both ranges due to combined absorption from Tb^{3+} and Eu^{3+}. Due to a very efficient energy transfer from Tb^{3+} to Eu^{3+} the phosphor exhibits solely red emission at Eu^{3+} concentration of 20% and higher. A method to determine energy transfer rates from rise time curves and emission spectra has been developed and was used to calculate the energy transfer efficiency and investigate the nature of the energy transfer mechanism. The energy transfer follows the dipole–dipole mechanism and the transfer efficiency is independent of the temperature but depends strongly on the Eu^{3+} concentration. Temperature-dependent excitation spectra revealed that Eu^{3+} $^7F_1$, $^7F_2$ and $^7F_3$ levels are thermally populated at room temperature and transitions originating from these levels can be observed.

By using TM:Eu^{3+} ceramics a full conversion of a 380 nm LED and reasonable conversion of a blue 465 nm LED was achieved. The quantum efficiency depends on the Eu^{3+} concentration and reached a maximum of 87% in $(Tb_{0.8}Eu_{0.2})_2Mo_3O_{12}$. These observations show that TM:Eu^{3+} is a very promising candidate as a radiation converter for warm-white pcLEDs and underline the potential of red line emitters for high efficiency pcLEDs with a very good CRI.

Acknowledgements

This work was generously financially supported by Merck KGaA, Darmstadt, Germany.

Notes and references

1 E. F. Schubert and J. K. Kim, *Science*, 2005, **308**, 1274.
2 S. C. Allen and A. J. Steckl, *Appl. Phys. Lett.*, 2008, **92**, 143309.
3 *LEDs for lighting applications*, ed. P. Mottier, ISTE Ltd, London, 2009.
4 Y. Narukawa, M. Ichikawa, D. Sanga, M. Sano and T. Mukai, *J. Phys. D: Appl. Phys.*, 2010, **43**, 354002.
5 M. Born and T. Jüstel, *Chem. Unserer Zeit*, 2006, **40**, 294.
6 R.-J. Xie and N. Hirosaki, *Sci. Technol. Adv. Mater.*, 2007, **8**, 588.
7 A. A. Setlur, *Electrochem. Soc. Interface*, 2009, **18**, 32.
8 R. Mueller-Mach, G. O. Mueller, M. R. Krames, H. A. Höppe, F. Stadler, W. Schnick, T. Jüstel and P. Schmidt, *Phys. Status Solidi A*, 2005, **202**, 1727.
9 P.-C. Hung and J. Y. Tsao, *J. Disp. Technol.*, 2013, **9**, 405.
10 A. Žukauskas, R. Vaicekauskas, F. Ivanauskas, H. Vaitkevičius and M. S. Shur, *Appl. Phys. Lett.*, 2008, **93**, 51115.
11 J. Y. Tsao, J. J. Wierer Jr, L. E. S. Rohwer, M. E. Coltrin, M. H. Crawford, J. A. Simmons, P.-C. Hung, H. Saunders, D. S. Sizov, R. Bhat and C.-E. Zah, in *III-Nitride Based Light Emitting Diodes and Applications*, ed. T.-Y. Seong, J. Han, H. Amano and H. Morkoc, Springer, Dordrecht, 2013, p. 11.
12 S. Adachi and T. Takahashi, *J. Appl. Phys.*, 2008, **104**, 23512.
13 F. Baur, A. Katelnikovas, S. Sakirzanovas, R. Petry and T. Jüstel, *Z. Naturforsch., B: J. Chem. Sci.*, 2014, **69**, 183.
14 *WinXPOW*, STOE & Cie GmbH, Darmstadt, Germany, 2011.
15 E. T. Keve, S. C. Abrahams, K. Nassau and A. M. Glass, *Solid State Commun.*, 1970, **8**, 1517.
16 L. H. Brixner, P. E. Bierstedt, A. W. Sleight and M. S. Licis, *Mater. Res. Bull.*, 1971, **6**, 545.
17 K. Nassau, J. W. Shiever and E. T. Keve, *J. Solid State Chem.*, 1971, **3**, 411.
18 S. C. Abrahams, C. Svensson and J. L. Bernstein, *J. Chem. Phys.*, 1980, **72**, 4278.
19 L. Vegard, *Z. Phys.*, 1921, **5**, 17.
20 A. Katelnikovas, J. Plewa, S. Sakirzanovas, D. Dutczak, D. Enseling, F. Baur, H. Winkler, A. Kareiva and T. Jüstel, *J. Mater. Chem.*, 2012, **22**, 22126.

21 P. S. Dutta and A. Khanna, *ECS J. Solid State Sci. Technol.*, 2013, **2**, R3153–R3167.
22 X. Liu, L. Li, H. M. Noh, B. K. Moon, B. C. Choi and J. H. Jeong, *Dalton Trans.*, 2014, **43**, 8814.
23 J.-Y. Chen, Q.-R. Zhang, T.-Y. Liu, Z.-X. Shao and C.-Y. Pu, *Chin. Phys. Lett.*, 2007, **24**, 1660.
24 W. Zhang, J. Sun, X. Wang, G. Shen and D. Shen, *CrystEngComm*, 2012, **14**, 3490.
25 H. Yamamoto, S. Shionoya and W. M. Yen, *Practical applications of phosphors*, CRC Press, Boca Raton, FL, 2007.
26 A. M. Srivastava and T. J. Sommerer, *Electrochem. Soc. Interface*, 1998, **7**, 28.
27 E. F. Schubert, *Light-emitting diodes*, Cambridge Univ. Press, Cambridge, 2010.
28 J.-C. G. Bünzli and S. V. Eliseeva, in *Lanthanide Luminescence: Photophysical, Analytical and Biological Aspects*, ed. P. Hänninen and H. Härmä, Springer-Verlag. Berlin, Heidelberg, 2011, p. 1.
29 L. J. Nugent, R. D. Baybarz and J. L. Burnett, *J. Phys. Chem.*, 1973, **77**, 1528.
30 E. Würzberg, *J. Chem. Phys.*, 1976, **64**, 1254.
31 X. L. Xiao, Y. Z. Cheng, J. Peng, M. M. Wu, D. F. Chen, Z. B. Hu, R. Kiyanagi, J. S. Fieramosca, S. Short and J. Jorgensen, *Solid State Sci.*, 2008, **10**, 321.
32 G. H. Dieke, H. M. Crosswhite and H. Crosswhite, *Spectra and energy levels of rare earth ions in crystals*, Interscience Publishers, New York, 1968.
33 M. O. Rodrigues, J. D. L. Dutra, L. A. O. Nunes, G. F. de Sá, W. M. de Azevedo, P. Silva, F. A. A. Paz, R. O. Freire and S. A. Júnior, *J. Phys. Chem. C*, 2012, **116**, 19951.
34 M. L. Debasu, D. Ananias, J. Rocha, O. L. Malta and L. D. Carlos, *Phys. Chem. Chem. Phys.*, 2013, **15**, 15565.
35 M. L. Debasu, D. Ananias, A. G. Macedo, J. Rocha and L. D. Carlos, *J. Phys. Chem. C*, 2011, **115**, 15297.
36 Y. Ruan, Q. Xiao, W. Luo, R. Li and X. Chen, *Nanotechnology*, 2011, **22**, 275701.
37 R. M. Ranson, E. Evangelou and C. B. Thomas, *Appl. Phys. Lett.*, 1998, **72**, 2663.
38 G. U. Caldiño, *J. Phys.: Condens. Matter*, 2003, **15**, 3821.
39 B. C. Joshi, R. Lohani and B. Pande, *Indian J. Pure Appl. Phys.*, 2001, **39**, 443.
40 P. I. Paulose, G. Jose, V. Thomas, N. V. Unnikrishnan and M. K. R. Warrier, *J. Phys. Chem. Solids*, 2003, **64**, 841.
41 R. Reisfeld, E. Greenberg, R. Velapoldi and B. Barnett, *J. Chem. Phys.*, 1972, **56**, 1698.
42 Y. Wang and D.-Y. Wang, *J. Electrochem. Soc.*, 2006, **153**, H166.
43 T.-W. Kuo, C.-H. Huang and T.-M. Chen, *Opt. Express*, 2010, **18**, A231.
44 J. Zhou and Z. Xia, *J. Mater. Chem. C*, 2014, **2**, 6978.
45 M. Müller and T. Jüstel, *J. Lumin.*, 2014, **155**, 398.
46 Z. Yang, S. Ma, H. Yu, F. Wang, X. Ma, Y. Liu and P. Li, *J. Alloys Compd.*, 2011, **509**, 76.
47 Z. Fen and T. Wanjun, *Opt. Mater.*, 2014, **37**, 561.
48 T. Jiang, X. Yu, X. Xu, H. Yu, D. Zhou and J. Qiu, *Opt. Mater.*, 2014, **36**, 611.
49 Z. Xia, J. Zhuang and L. Liao, *Inorg. Chem.*, 2012, **51**, 7202–7209.
50 Z. Xia, J. Zhuang, A. Meijerink and X. Jing, *Dalton Trans.*, 2013, **42**, 6327.
51 V. V. Atuchin, A. S. Aleksandrovsky, O. D. Chimitova, A. S. Krylov, M. S. Molokeev, B. G. Bazarov, J. G. Bazarova and Z. Xia, *Opt. Mater.*, 2014, **36**, 1631–1635.
52 *Color Calculator*, Osram Sylvania, Danvers, MA, USA, 2011.
53 M. Wiegel and G. Blasse, *J. Solid State Chem.*, 1992, **99**, 388–394.